Broadband photoluminescence toward NIR II region and stable green ceramic pigments based on a novel $NaBaScSi_2O_7$: *x*Cr silicate phosphor

Xuejiao Wang,[a*] Sihan Yang,[a] Feng Jiang,[b] Jiantong Wang,[a] Changshuai Gong,[a] Ji-Guang Li[c*]

[a]*College of Chemistry and Materials Engineering, Bohai University, Jinzhou, Liaoning 121007, China*

[b]*Department of Material Science and Engineering, Jingdezhen Ceramic University, Jingdezhen 333000, China*

[c]*Research Center for Functional Materials, National Institute for Materials Science, Tsukuba, Ibaraki 305-0044, Japan*

*Corresponding author

Dr. Xuejiao Wang
Bohai University
Jinzhou, China
Tel: +86-416-3400708
E-mail: wangxuejiao@bhu.edu.cn

Dr. Ji-Guang Li
National Institute for Materials Science
Tsukuba, Japan
Tel: +81-29-860-4394
E-mail: li.jiguang@nims.go.jp

Abstract

Cr^{3+}-activated NIR phosphors are the most promising materials for commercialization, however, the emission of most Cr^{3+}-activated phosphors typically located in the NIR I region. It is challenging to achieve luminescence towards NIR II region (> 900 nm) *via* Cr^{3+} doping. In this work, a novel Cr^{3+} activated $NaBaScSi_2O_7$ phosphor which shows broadband emission at 974 nm with a FWHM reaching 140 nm under 493 nm blue light excitation is reported. The emission position exceeds that of most NIR phosphors activated by Cr^{3+}. The underlying mechanism for the encouraging phenomenon was attributed to the strong charge polarization caused by the intrinsic local coordination environment where Cr^{3+} are located, which was confirmed by charge differential density (CDD) and the electron localization function (ELF) analysis. The properties of phosphors were systematically investigated. The performances of the fabricated NIR pc-LED device in the fields of night vision and non-invasive imaging were evaluated. Remarkably, the samples show bright green color and good color properties, and the application of the studied materials in stable green ceramic pigments was explored.

Keywords: Silicates, Broadband near-infrared, Cr^{3+} doping, Photoluminescence, Ceramic pigments

1. Introduction

Near-infrared spectroscopy has been widely used in remote control, night vision, near-infrared imaging and biomedical applications due to its safety, non-destructive and suitable penetrating characteristics. [1–4] Common near-infrared light source devices include halogen tungsten lamps, laser diodes, organic LEDs, etc., however, the inherent limitations of poor stability, slow response speed, and demanding working environment conditions limit their intelligent applications in multiple fields. [5–7] In contrast, phosphor converted light-emitting diode (pc-LED) have gained attention due to their spectral tunability, small size, and high integration capabilities. [8,9] In fields such as medical diagnostics and food analysis, broad-band near-infrared emission with a FWHM greater than 100 nm is more attractive compared to narrow-band emission. This is due to multiple functional groups (O-H, C-H, N-H) present in human tissues and food may interact with specific wavelengths of light in the near-infrared region. [10,11] Therefore, broad-band near-infrared light sources can provide more accurate analysis results, the key to this technology is the synthesis of broad-band near-infrared phosphors.

The activators are critical in the design of near-infrared phosphors. Currently, it is mainly focused on the use of rare earth ions (typically Nd^{3+}, Yb^{3+}, Pr^{3+}, Tm^{3+}), or transition metal ions (typically Cr^{3+}, Ni^{2+}) to explore and excavate near-infrared phosphors. [12–16] It is reported that the 4*f*-4*f* transition of trivalent rare earth ions shows narrow-band near-infrared emission and weak absorption, [17] while the excitation position of Ni^{2+} doped near-infrared phosphors is usually located in the ultraviolet region. [18] At this point, Cr^{3+} stands out as a luminescent center due to its effective excitation by blue light and its capability to achieve tunable broadband near-infrared emission within the range of 700-1200 nm. The electronic transitions of the 3*d* orbitals of Cr^{3+} are notably affected by variations in the crystal field environment, and the tuning of the luminescence of Cr^{3+} can be realized by regulating the crystal field, [19–21] thus making Cr^{3+} an excellent candidate for the activator of broadband near-infrared phosphors.

Currently, the design and development of novel Cr^{3+}-doped near-infrared phosphors are steadily advancing. However, their emission mainly resides in the NIR I region of 650-900 nm (Table S1, ESI†). This region faces challenges such as reduced emission intensity and inadequate spatial resolution. In contrast, the NIR II region (1000-1700 nm) encompasses vibrational frequencies of multiple functional groups, making it highly promising for applications in bio-imaging and non-destructive analysis. Moreover, NIR II offers advantages such as strong penetration, high sensitivity, and superior spatial resolution. [7,22] In addition, the emission range of broad-band phosphors towards NIR II is highly consistent with the low-cost In-GaAs detection range of 900-1700 nm. [23] Therefore, it is of great significance to develop Cr^{3+}-doped broad-band phosphors with emission wavelengths (> 900 nm) towards NIR II region. Building upon this foundation, the focus of this study is to regulate the luminescence spectrum of Cr^{3+}, locate its luminescence within the NIR II region, while simultaneously achieving the desired superior performance. At present, the recognized effective spectral regulation methods include: (1) Crystal field engineering, which realizes the regulation of the crystal field and the local coordination environment of the polyhedron where Cr^{3+} is located by cation substitution or ion pair substitution; [24] (2) Multi-site luminescence, which provides multiple octahedral sites for Cr^{3+} in the lattice, and the spectra of different luminescent centers are overlapped to achieve spectral broadening; [25,26] (3) Energy transfer, by constructing energy transfer from Cr^{3+} to Ni^{2+}, Yb^{3+}, Er^{3+}, Mn^{2+}, to broaden the spectrum and realize the regulation of near-infrared emission position; [27] alternatively, Ce^{3+}, Bi^{3+} are used as donor ions to transfer energy to the acceptor Cr^{3+} to achieve luminescence enhancement. [28]

Silicate-based phosphors have garnered widespread attention for their superior physical and chemical stability compared to other types such as nitride and fluoride phosphors. They offer advantages such as moisture resistance, oxidation resistance, and not interacting with the contacting

resins during the encapsulation process. After detailed structure and luminescence properties investigation, we found that the $ABScSi_2O_7$ (A = Na, K, Rb, B = Sr, Ba) scandium complex silicate which has unique structural advantages was first reported in 2010. [29] The [ScO_6] octahedra therein provide a suitable crystal field for the activator Cr^{3+}, and the distinctive Sc-O-Si bonding configuration would influence the electric field environment around Cr^{3+} luminescent centers due to local charge polarization, which makes $ABScSi_2O_7$ promising host for Cr^{3+} to achieve luminescence towards longer region of NIR II. $NaBaScSi_2O_7$ is a typical example of this structure, phosphors with $NaBaScSi_2O_7$ as the matrix lattice and Eu^{2+}, Tb^{3+}, Ce^{3+} as activators have been successively developed recently, [30–32] and the developed phosphors show promising photoluminescence performance. However, doping Cr^{3+} in $NaBaScSi_2O_7$ structure to achieve broad-band NIR emission has never been reported.

In this work, $NaBaScSi_2O_7$: $x$$Cr^{3+}$ phosphors were designed and synthesized. The weak crystal field environment provided by the $NaBaScSi_2O_7$ matrix allows Cr^{3+} to exhibit a broad-band emission at 974 nm, which is longer than most NIR phosphors using Cr^{3+} as activator reported so far. The luminescence mechanism and the influence of the local coordination environment of the matrix on the emission of Cr^{3+} were systematically studied. In addition, the obtained $NaBaScSi_2O_7$: $x$$Cr^{3+}$ powders exhibit bright green color, we exploratively investigated the application of the product as green ceramic pigment since the synthetic inorganic green pigments are quite limited to garnet-structured Victoria green, spinel-structured, and composite zircon pigments. [33–35] We anticipate that $NaBaScSi_2O_7$: $x$$Cr^{3+}$ will demonstrate excellent performance on a dual-functional platform for both pc-LEDs and ceramic pigments.

2. Experimental section

2.1. Reagents and synthesis

Aladdin Industrial Corporation (Shanghai, China) supplied the Na_2CO_3 (99.9%), $BaCO_3$ (99.9%),

Sc_2O_3 (99.9%), SiO_2 (99.99%), and Cr_2O_3 (99.99%), which were utilized without further purification. $NaBaScSi_2O_7$: $x$$Cr^{3+}$ (x=0.0025−0.10) phosphors were prepared by the traditional solid-state reaction approach. Stoichiometrically calculated raw materials were pulverized in an agate mortar with alcohol for twenty minutes, thoroughly mixed, and subsequently relocated to a corundum crucible. This preparation was subjected to heating at 1300 °C for 6 h in the N_2 atmosphere, and the as-prepared phosphors were obtained after cooling.

2.2. Glazing process

In order to evaluate the coloring performance of $NaBaScSi_2O_7$: $x$$Cr^{3+}$ in the application of stable ceramic pigments, the prepared powder samples (10 wt%) were uniformly mixed with commercial transparent glazes and glazed on traditional ceramic body, following 1200 °C sintering (2 h). The transparent glaze and ceramic matrix used in the experiment were from Peiyintang Ceramic Glaze Co., Ltd. (Jingdezhen, China).

2.3. Characterization

Sample crystalline phases were discerned using an X-ray diffractometer (Model Ultima IV, Rigaku, Tokyo, Japan) with Cu-K_α (λ = 0.15406 nm) radiation in 2θ = 5−70° range. The step scan range of the diffraction data collected for the Rietveld refinement was 2θ of 5°−100°.Furthermore, the morphology and elemental distribution of particles were investigated using FE-SEM (model Tescan MIRA LMS, Tesken). X-ray photoelectron spectroscopy (XPS) analysis was conducted using a Thermo Scientific K-Alpha analyzer (model Thermo ESCALAB 250Xi, Thermo Fisher Scientific, USA). PL and PLE spectra were measured using an FLS1000 Photoluminescence Spectrometer (Edinburgh Instruments Ltd., Herrsching am Ammersee, Britain). The configured lifetime testing unit was used to monitor the fluorescence decay curves. The spectrophotometer of the TAP-02 high-temperature controller was configured for the test of the temperature-dependent luminescence spectra. Additionally, the chromaticity values (CIE $L^*a^*b^*$) for the pigments were measured using an automatic whiteness meter with tungsten and deuterium lamps as light sources (model WSD-3 color system).

Where L^* indicates luminance, 0−100 corresponds to black to white; a^* corresponds to green ($-a^*$) to red (a^*); and b^* ranges to blue ($-b^*$) to yellow (b^*).

2.4. Computational Procedure

Calculations were performed using density functional theory (DFT) with the Vienna ab initio simulation package (VASP) package, employing projected augmented wave potentials and a plane wave basis. [36] The GGA-PBE function was used to describe the exchange-correlation energy. The cutoff energy of the plane wave basis was set at 500 eV, and a 2×2×2 Gamma k-grid was employed in the calculation. The convergence criteria were set for total energy change at 1.0×10^{-4} eV and atomic force magnitude at 5.0×10^{-2} eV/Å.

3. Results and discussion

3.1. XRD characterization and structure analysis

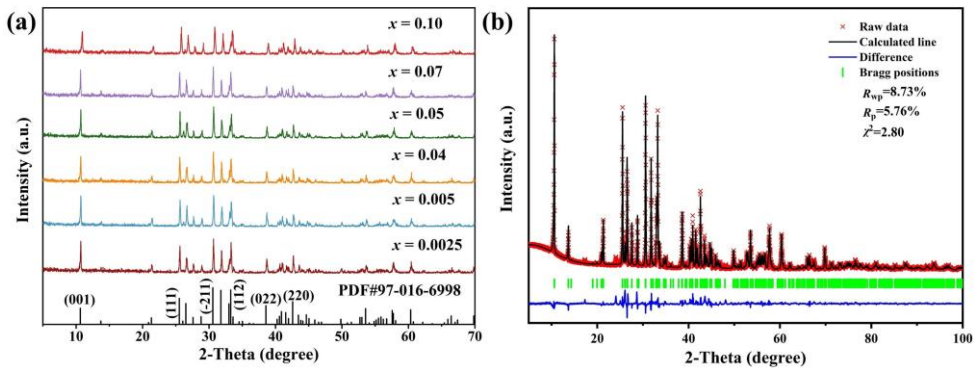

Fig. 1 (a) XRD patterns of $NaBaScSi_2O_7$: xCr^{3+} (x = 0.0025−0.10). (b) Rietveld refinement result for $NaBaSc_{0.95}Si_2O_7$: $0.05Cr^{3+}$.

X-ray diffraction analyses were performed on $NaBaScSi_2O_7$: xCr^{3+} (x = 0.0025−0.10) samples, as presented in Fig. 1a, it can be clearly observed that the diffraction peaks of the series of samples can be well correspond to the $NaBaScSi_2O_7$ (PDF#97-061-6998) standard card. In order to further determine the phase purity and obtain the crystallographic data, we performed Rietveld refinement for a typical $NaBaSc_{0.95}Si_2O_7$: $0.05Cr^{3+}$ sample using the GSAS software package (Fig. 1b). Comprehensive details concerning the refinement can be found in Table S2 (ESI†). The reliability parameters of the refinement were R_p = 5.76%, R_{wp} = 8.73%, R_{exp} = 3.11% and χ^2 = 2.80 respectively,

this result further proves the high level of phase purity of the samples.

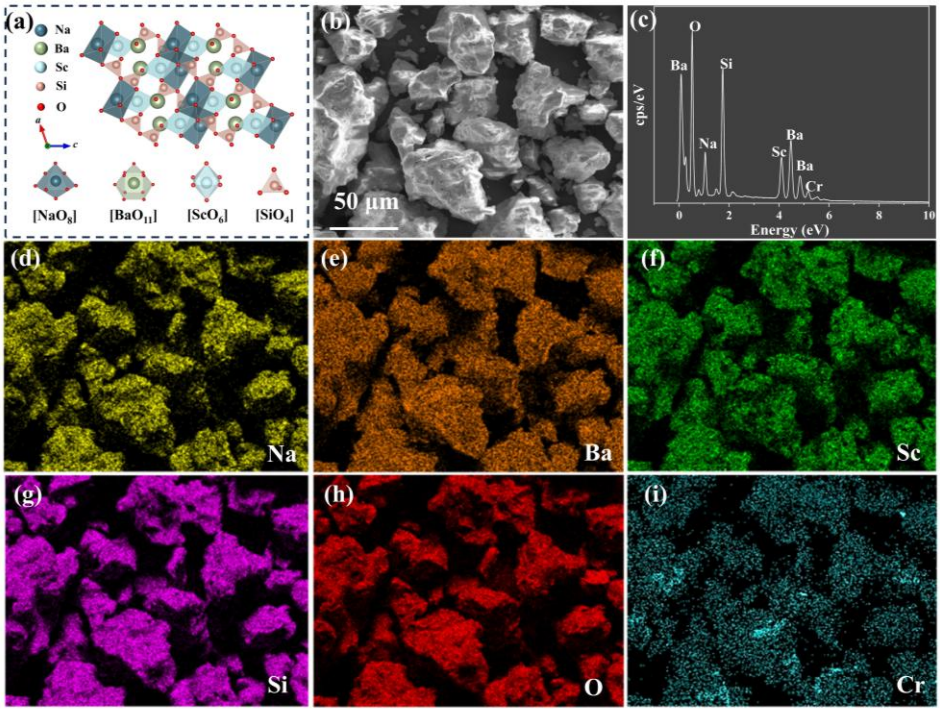

Fig. 2 (a) The crystal structure of $NaBaScSi_2O_7$, (b) FE-SEM image, (c) energy dispersive spectrum (EDS) analysis, and (d−i) element mapping of $NaBaSc_{0.95}Si_2O_7$: $0.05Cr^{3+}$ sample.

Fig. 2a shows the crystal structure of $NaBaScSi_2O_7$, the lattice belonging to the monoclinic $P2_1/m$ space group. In this structure, $[ScO_6]$ octahedra and $[SiO_4]$ tetrahedra are alternately connected by sharing oxygen atoms to form a three-dimensional network structure, while Na^+ and Ba^{2+} are located in the voids of the network and arranged along the *c*-axis in the order of Ba-Na-Ba. $NaBaScSi_2O_7$ provides three different cationic sites for the activator occupancy, namely, $[ScO_6]$, $[BaO_{11}]$, and $[NaO_8]$. According to previous reports, the ionic radii of Na^+, Ba^{2+} and Sc^{3+} are 1.180 Å (CN = 8), 1.470 Å (CN = 9) and 0.745 Å (CN = 6), respectively, while the radius of Cr^{3+} is 0.615 Å (CN = 6).[37] Considering the factors of radius, valence state, and coordination number of polyhedrons, we believe that Cr^{3+} mainly occupies the $[ScO_6]$ site in the host. Fig. 2b and c shows the FE-SEM image and EDS spectrum of $NaBaSc_{0.95}Si_2O_7$: $0.05Cr^{3+}$. These results reveal that irregular particle morphology characterized by a rough surface and particle size ranging from 20 to 50 μm, and the characteristic peaks of Na, Ba, Sc, Si, O and Cr can be clearly observed. From the elemental mapping (Fig. 2d−i), it

can be clearly seen that all the elements, including the doped activator Cr^{3+}, are uniformly distributed in the sample, which also proves that we have obtained the sample with high purity.

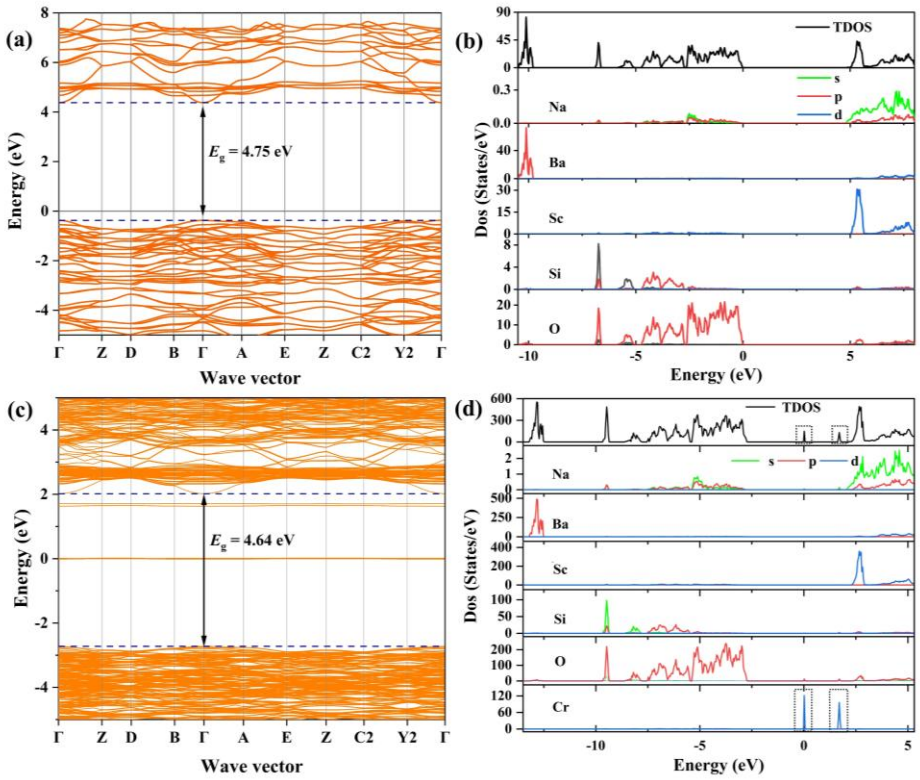

Fig. 3 Band structure and total and partial DOS of (a−b) pure $NaBaScSi_2O_7$ and (c−d) $NaBaSc_{0.95}Si_2O_7$: $0.05Cr^{3+}$.

We calculated the energy band structures (Fig. 3a, Fig. 3c) and density of states distributions (Fig. 3b, Fig. 3d) of $NaBaScSi_2O_7$ and $NaBaSc_{0.95}Si_2O_7$: $0.05Cr^{3+}$ using first-principles calculations *via* the VASP software. The bandgap (E_g) of $NaBaScSi_2O_7$ is calculated to be 4.75 eV, which is sufficiently large to indicate that this lattice is capable of providing a suitable band gap for the transition of the Cr^{3+} 3*d* orbital electrons. The minimum conduction band and the maximum valence band are both situated at the Γ point in the Brillouin zone, indicating that the material has a direct bandgap. As can be seen in Fig. 2b, the bottom of the conduction band is affected by the 3*d* state of Sc and the top of the valence band is mainly contributed by the 2*p* state of O before doping. After doping with the activator, two distinct peaks clearly appear in the middle of the band gap, which are attributed to the 3*d* states of the doped Cr^{3+}. The introduction of Cr^{3+} creates new electronic states that affect the

electronic structure of the material. It also proves that the lattice can provide a suitable band gap for Cr^{3+} to realize broadband NIR emission.

3.2. Broadband photoluminescence toward NIR II region from the $NaBaScSi_2O_7$: *x*Cr phosphor

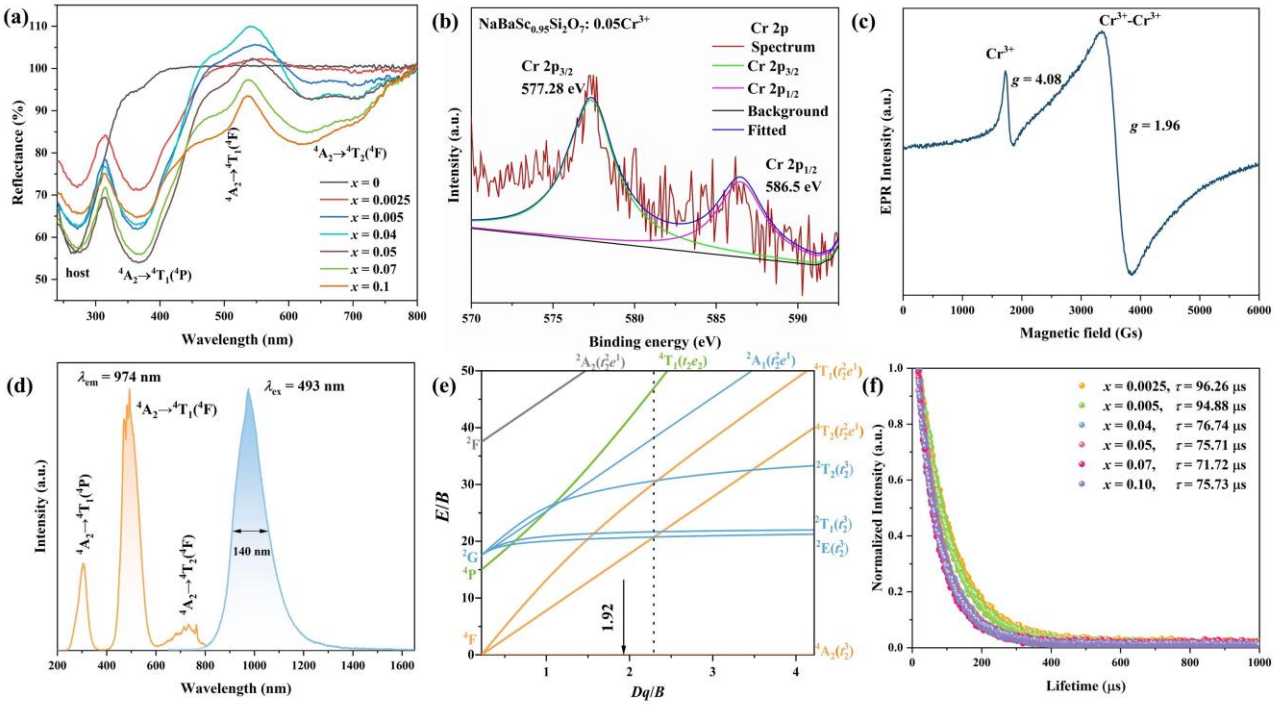

Fig. 4 (a) Diffuse reflectance spectra of $NaBaSc_{1-x}Si_2O_7$: xCr^{3+}, (b) high-resolution XPS spectra of Cr 2*p* orbital. (c) EPR spectrum, and (d) PLE and PL spectra of $NaBaSc_{0.95}Si_2O_7$: $0.05Cr^{3+}$. (e) Tanabe-Sugano diagram for Cr^{3+} ions in octahedral coordination, (f) the decay curves of the main emission (974 nm) of $NaBaSc_{1-x}Si_2O_7$: xCr^{3+}.

The diffuse reflectance spectra of the series of $NaBaSc_{1-x}Si_2O_7$: xCr^{3+} (x = 0−0.1) samples are displayed in Fig. 4a. The $NaBaScSi_2O_7$ matrix showed absorption band in 230−330 range. Compared with the host $NaBaScSi_2O_7$, the Cr^{3+} doped samples showed new absorption peaks at 300−440 nm, 440−535 nm, and 535−800 nm, which corresponded to the transitions of Cr^{3+} from the ground state $^4A_2$ to $^4T_1(^4P)$, $^4T_1(^4F)$, and $^4T_2(^4F)$, respectively. Additionally, the Kubelka−Munk function is applicable for determining the optical bandgap of the samples: [21]

$$F(R) = \frac{(1-R)^2}{2R} \quad (1)$$

$$Ah\nu = c\left(h\nu - E_g\right)^{1/2} \quad (2)$$

$$[h\nu F(R_\infty)]^{1/n} = A\left(h\nu - E_g\right) \quad (3)$$

In the equations, R is the reflectance coefficient, c denotes the absorption constant, hv is the photon energy, $F(R\infty)$ corresponds to the absorption, E_g indicates the optical band gap, while n is a constant with n = 1/2 for direct allowed transition, n = 3/2 for direct forbidden transition, n = 2 for indirect allowed transition, and n = 3 for indirect forbidden transition. [38] The correlation between hv and $[F(R\infty)hv]^2$ for $NaBaScSi_2O_7$ and $NaBaSc_{0.95}Si_2O_7$: $0.05Cr^{3+}$ are shown in Fig. S1a−b (ESI†). The first rising edge in Fig. S1a corresponds to the intrinsic low-energy defect absorption state of the matrix, as confirmed by thermoluminescence analysis in Fig. S??. After doping with Cr^{3+}, new energy levels are introduced into the electronic structure, which is reflected in the rising edge at a lower energy in Fig. S1b. In order to obtain more accurate E_g values, the linear portions of the $[F(R\infty)hv]^2$ *versus* hv curves were extrapolated to the pre-bandgap absorption minimum instead of the x-axis according to Makuła et al. [39] and the E_g values for $NaBaScSi_2O_7$ and $NaBaSc_{0.95}Si_2O_7$: $0.05Cr^{3+}$ were calculated to be 5.38 eV and 5.29 eV respectively. The slight reduction in the band gap upon Cr^{3+} doping is consistent with the band structure analysis from first-principles calculations. The valence of the Cr element is decisive for its luminescence since the Cr^{3+} and Cr^{4+} are both reported to show luminescence in different hosts. Hence, the XPS technique was utilized to assess the oxidation states of the chromium element. Fig. S2 (ESI†) presents the XPS survey spectra for the $NaBaSc_{0.95}Si_2O_7$: $0.05Cr^{3+}$ sample. It is apparent that, aside from the C 1*s* level, all other spectral features can be traced back to the inherent elements of $NaBaSc_{0.95}Si_2O_7$: $0.05Cr^{3+}$. Fig. 4b illustrates the high-resolution XPS spectra of the Cr 2*p* orbital. Due to the minimal doping level, the resulting spectrum exhibits lower resolution. The spectrum can be approximately fitted into two sub-peaks at binding energies of 586.5 eV and 577.28 eV, which align with the Cr $2p_{1/2}$ and Cr $2p_{3/2}$ orbitals, respectively. The experimental data are closer to the binding energy of Cr^{3+} than that of Cr^{4+}, which confirms the presence of Cr in the sample in the state of 3+. [40] Electron paramagnetic resonance (EPR) is a crucial method for examining

the local coordination environment of Cr^{3+}, and the EPR spectrum of $NaBaSc_{0.95}Si_2O_7$: $0.05Cr^{3+}$ is displayed in Fig. 4c. The EPR response signal at g = 1.96 is due to the exchange interaction of Cr^{3+}-Cr^{3+} pairs, while the asymmetric signal at g = 4.08 is associated with the isolated Cr^{3+} occupying octahedral positions.[41] According to the previous literature, the intensity of the Cr^{3+}-Cr^{3+} pair signal in the EPR spectrum is positively correlated with the energy migration of the Cr^{3+} in the host matrix, and the enhanced signal may promote the redshift of the Cr^{3+} luminescence spectrum.[42] In other words, the strong Cr^{3+}-Cr^{3+} pair signal observed in Fig. 4c covering a wide magnetic field range may be one of the factors responsible for the broadband emission of Cr^{3+} in $NaBaScSi_2O_7$ toward NIR II region.[42] Fig. 4d shows the normalized PLE and PL spectra of $NaBaSc_{0.95}Si_2O_7$: $0.05Cr^{3+}$. It is evident that there are three excitation bands observed, originating from the specific electronic transitions of Cr^{3+}, located at 200−380 nm, 380−600 nm, and 660−800 nm, respectively. It was noted that the positions of $^4A_2 \rightarrow {}^4T_1$ (^4F) transition, as observed in both the PLE spectrum and diffuse reflectance spectrum, were consistent with each other. For the $^4A_2 \rightarrow {}^4T_1$ (^4P) transition, position deviation was observed and this may be due to the influence of strong host absorption as shown in Fig. 4a. Similarly, the $^4A_2 \rightarrow {}^4T_2$ (^4F) transition also showed difference in position, which may be due to strong charge polarization within the $NaBaScSi_2O_7$ lattice, leading to a downshifting of the $^4T_2$ level. Therefore, in both the excitation and diffuse reflectance spectra, the $^4A_2 \rightarrow {}^4T_2$ (^4F) transition showed a red shift. The PLE spectrum was obtained by monitoring the strongest emission of Cr^{3+}, and the position of PLE band may be more sensitive to slight changes in the excited state energy levels. In contrast, diffuse reflection spectrum reflects the optical absorption of the whole host, resulting in less change in the peak position of the specific transition. Under excitation at the strongest excitation of 493 nm, the sample exhibits broad-band emission at 974 nm with a FWHM of 140 nm. It is encouraging to note that compared to the most Cr^{3+}-doped near-infrared phosphors reported so far, $NaBaSc_{0.95}Si_2O_7$: $0.05Cr^{3+}$ shows a

noticeable red shift in emission position toward NIR II region. Analyzing the crystal field strength is a vital component in the study of the luminescence characteristics of Cr^{3+} ions. This analysis entails the examination of the $3d^3$ level splitting of Cr^{3+} within an octahedral field, as illustrated by the Tanabe-Sugano diagram (Fig. 4e). The octahedral crystal field parameters *Dq* and Racah parameters *B* are important parameters to characterize the crystal field strength. Typically, when *Dq*/*B* falls below 2.3, Cr^{3+} is presumed to be located in the weak crystal field environment, which leads to broadband near-infrared emission. *Dq* and *B* can be derived from the equations provided: [43]

$$10Dq = E(^4T_2 \rightarrow {}^4T_1) \quad (4)$$

$$\frac{Dq}{B} = \frac{15(x-8)}{(x^2-10x)} \quad (5)$$

$$x = [E(^4A_2 \rightarrow {}^4T_1) - E(^4A_2 \rightarrow {}^4T_2)/Dq] \quad (6)$$

The computed values of *Dq*, *B*, and *Dq*/*B* for $NaBaScSi_2O_7$: Cr are about 1367.99 cm^{-1}, 717.84 cm^{-1}, and 1.92, respectively. The smaller value of *Dq*/*B* indicates that the $^4T_2 \rightarrow {}^4A_2$ transition predominates, resulting in broadband NIR emission. From the series of emission spectra of $NaBaSc_{1-x}Si_2O_7$: xCr^{3+} (x = 0.0025−0.1) in Fig. S3a (ESI†), the emission intensity is observed to increase gradually with Cr^{3+} concentration, reaching the maximum when x = 0.05, and subsequently diminishing as the concentration continues to rise. The concentration quenching phenomenon is typically caused by energy transfer between activator ions. Therefore, to investigate the mechanism of concentration quenching, it is necessary to calculate the energy transfer critical distance R_c. The R_c is calculated to be 18.29 Å from eqn. S1 (ESI†). According to empirical rules, when the distance exceeds 5 Å, it is assumed that electric multipole interactions dominate. Next, based on Dexter's theory, the specific type of electric multipole interaction can be determined using eqn. S2 (ESI†). The key is the determination of the θ-value, which can correspond to several possible modes: non-radiative energy transfer between neighboring activator ions (θ = 3), dipole-dipole (θ = 6), dipole-quadrupole (θ = 8), and quadrupole-quadrupole (θ = 10). Fig. S3b (ESI†) shows the linear relationship between log(*I*/*x*)

and log$x$, from which the θ-value is determined to be 3.3. This indicates that the dominant type of electric multipole interaction is non-radiative energy transfer among the nearest-neighbor ions. The decay curves of the main emission (λ_{ex} = 493 nm, λ_{em} = 974 nm) of the $NaBaSc_{1-x}Si_2O_7$: xCr^{3+} phosphors at room temperature are illustrated in Fig. 4f, and can be fitted by the double-exponential decay equation: [44]

$$I_t = A_1 exp\left(\frac{-t}{\tau_1}\right) + A_2 exp\left(\frac{-t}{\tau_2}\right) \quad (7)$$

where I_t denotes the luminescence intensity, A_1 and A_2 represent the fitting constants, and τ_1 and τ_2 are the decay times for the exponential components, the specific parameters are given in Table S3 (ESI†). By using eqn. 8 the average lifetime can be obtained:

$$\tau_{avg} = \frac{A_1\tau_1^2 + A_2\tau_2^2}{A_1\tau_1 + A_2\tau_2} \quad (8)$$

It can be found that as the value of x increases, the average lifetime of $NaBaSc_{1-x}Si_2O_7$: xCr^{3+} (x = 0.0025−0.10) shows an overall decreasing trend, with slight fluctuations.

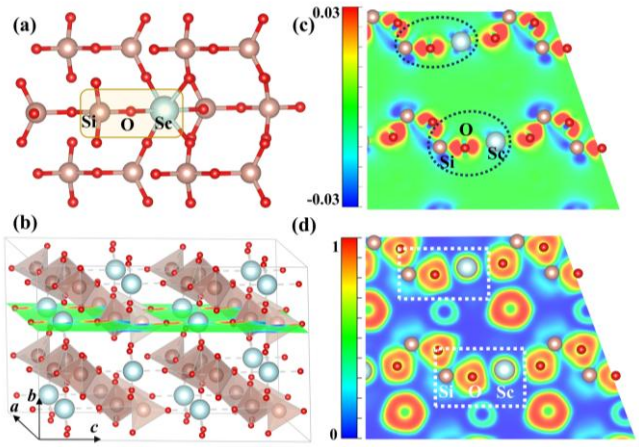

Fig. 5 (a) The schematic diagram of Sc-O-Si bonding configuration in $NaBaScSi_2O_7$ crystal structure; (b) the schematic diagram of the slice plane; (c) the charge differential density (CDD) analysis; and (d) the electron localization function (ELF) analysis.

It is known that the luminescent properties of the phosphors are closely related to their crystal structure. In $NaBaSc_{1-x}Si_2O_7$: xCr^{3+} phosphors, the observed emission toward NIR II region is closely related to the local coordination environment of Cr^{3+} ions. The crystal structure details illustrated in Fig. 5a exhibit that each vertex of isolated [ScO_6] octahedra shares oxygen atoms with the [Si_2O_7]

groups. Due to the electronic configuration of Si and O atoms and relatively similar electronegativity (Si = 1.887, O = 3.758, Sc = 1.347), [45] it means the formation of strong Si-O covalent bonds, thereby imparting strong ionic character between Sc and the shared oxygen atoms. The charge density differences (CDD) analysis and electron localization function (ELF) analysis provide supporting instructions, with the selected slicing plane as depicted in Fig. 5b. Fig. 5c shows a charge density difference (CDD) plot, which reveals the changes in electron density during the bonding process as well as the nature of the chemical bonds. In this diagram, negative values indicate electron loss, while positive values represent electron enrichment. The high charge density between Si and O indicates strong covalent interactions between them, whereas there is no overlap between Sc and O, confirming the strong ionic nature of the Sc-O bond. [46,47] The electron localization function (Fig. 5d) shows a similar trend. Obviously, the electron clouds around the shared oxygen atoms show irregular shapes. Compared to the vicinity of Sc atoms, the higher electron density between Si and O suggests that the strong covalent Si-O bonds exert a greater attraction on the electrons around the shared oxygen atoms, which leads to the distortion of the electric field environment around the Cr^{3+} and the symmetry of the [Cr/ScO_6] polyhedron is reduced by the influence of high charge polarization. [48,49] According to the crystal field theory, in the regular octahedral coordination environment, the d-orbital of Cr^{3+} will split into the doublet e_g with high energy ($d_{x^2-y^2}$, d_{z^2}) and the triplet t_{2g} with low energy (d_{xy}, d_{xz}, d_{yz}). The energy difference between two splitting energy levels is known as the crystal field splitting energy, which also represents the energy gap between the $^4T_2$ state and the $^4A_2$ state. When the symmetry of the Cr^{3+} octahedron is diminished by high charge polarization, the e_g and t_{2g} levels further split, leading to a reduction in the crystal field splitting energy. This implies a narrowing of the energy gap between the $^4T_2$ state and the ground state, indicating that the emission of Cr^{3+} shifts towards the longer wavelength NIR II region. [26,50]

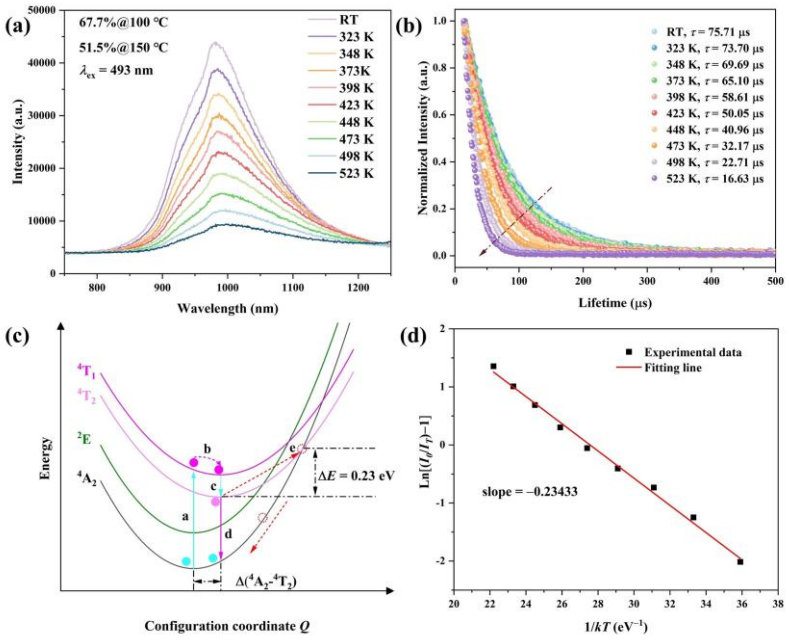

Fig. 6 (a) Temperature-dependent emission spectra; (b) decay curves of the 974 nm emission upon 493 nm excitation at different temperatures; (c) the schematic configuration coordinate diagram; and (d) plot of ln[(I_0/I_T)−1] *versus* 1/*kT* of the $NaBaSc_{0.95}Si_2O_7$: $0.05Cr^{3+}$ phosphor.

Fig. 6a shows the emission spectra of $NaBaSc_{0.95}Si_2O_7$: $0.05Cr^{3+}$ obtained from room temperature to 523 K. The emission intensity of $NaBaSc_{0.95}Si_2O_7$: $0.05Cr^{3+}$ gradually decreases with the increasing temperature, while the peak position of the spectra remains relatively unchanged. The luminescence intensity at 100 °C can be maintained at 67.7% at room temperature, and can be maintained at 51.5% when the temperature rises to 150 °C. Typically, longer-wavelength emitting phosphors correspond to electronic excited states with lower energy (i.e., smaller energy gaps). In this case, the electrons have lower energy and are more likely to interact with lattice vibrations (phonons). As the temperature increases, stronger electron-phonon coupling leads to more electrons losing energy through non-radiative transitions, which typically results in poorer thermal stability. Compared to phosphors with similar emission wavelengths, as exemplified by $NaInGe_2O_6$: Cr^{3+} (43%@150 ℃, λ_{em} = 935 nm), $LiIn_2SbO_6$: Cr^{3+} (<10%@150 ℃, λ_{em} = 965 nm), and $InTaO_4$: Cr^{3+} (<5%@150 ℃, λ_{em} = 975 nm), [51–53] $NaBaSc_{0.95}Si_2O_7$: $0.05Cr^{3+}$ demonstrates good thermal stability. Investigating the temperature-dependent decay behavior of the phosphor is also crucial for evaluating its performance, as illustrated in Fig. 6b. The decay curves can be well-fitted to the double-exponential function by eqns. 7 and 8.

Table S4 (ESI†) provides the detailed fitting results. We observed that as the temperature increases, the luminescence lifetime gradually decreases from 75.71 μs to 16.63 μs. This is due to the elevated temperature enhances more interactions between electrons and phonons, which in turn leads to an increase in the non-radiative transition rate. [54] The schematic diagram of the configuration coordinate curve of the Cr^{3+} transition process in Fig. 6c provides a more intuitive understanding of thermal quenching behavior. At room temperature, the main electron pathways of the Cr^{3+} primarily involve processes a−d, which can be summarized as follows: The electrons are initially excited by 493 nm blue light, transitioning from the $^4A_2$ level to the $^4T_1(^4F)$ level. Subsequently, they undergo vibrational relaxation to reach the lowest $^4T_1(^4F)$ excited state and further relax to the $^4T_2(^4F)$ level. Finally, they radiatively transition back to the $^4A_2$ ground state, emitting near-infrared light. As the ambient temperature increases, electrons located at the $^4T_2$ energy level can transfer to the intersection between the $^4A_2$ and the $^4T_2$ levels through the additional activation energy ΔE, and then undergo non-radiative relaxation back to the ground state, leading to thermal quenching behavior. Therefore, the ΔE value is an important index to evaluate thermal stability. It represents the energy required for the electron to overcome the energy barrier and can be calculated according to the following formula: [9]

$$I_T = \frac{I_0}{1+A*e^{(-\Delta E/kT)}} \quad (9)$$

where I_T and I_0 denote the intensity at a given temperature and initial intensity in the spectrum, respectively, and k is the Boltzmann constant. The horizontal and vertical coordinates are designed according to the eqn. 9. The slope from the linear fit corresponds to the thermal activation energy (ΔE), as illustrated in Fig. 6d. For $NaBaSc_{0.95}Si_2O_7$: $0.05Cr^{3+}$, the ΔE is 0.23 eV.

3.3. Application and performance of the $NaBaScSi_2O_7$: *x*Cr silicate phosphor in NIR pc-LED and stable green ceramic pigment

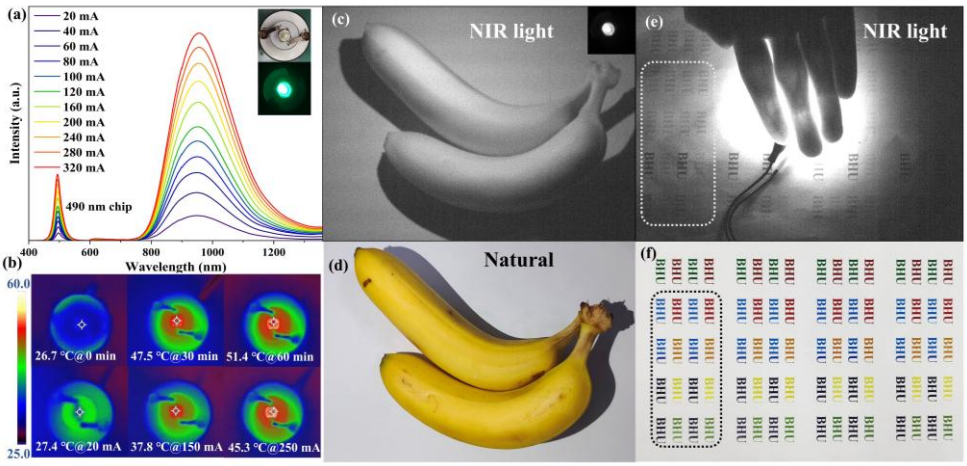

Fig. 7 (a) EL spectra of fabricated NIR pc-LED (20−320 mA), the inset is an image of a NIR pc-LED device. (b) Time-dependent thermographs of the NIR pc-LED device, and thermographs of the device at different driven currents from 20 to 250 mA. (c, e) Photographs taken in the near-infrared and (d, f) visible cameras, demonstrate the application of the device in night vision and perspective.

NIR pc-LEDs were fabricated by combining $NaBaSc_{0.95}Si_2O_7$: $0.05Cr^{3+}$ with a 493 nm chip. Fig. 7a demonstrates the electroluminescence spectra at different currents, with insets illustrating the photographs of the devices with the current on and off, and the emission intensity is gradually enhanced as the driving current is elevated from 20 mA to 320 mA. As shown in Fig. 7b, the fabricated NIR pc-LED device maintained an operational temperature of 51.4 °C after continuous operation for 60 minutes at a driving current of 250 mA, indicating its suitability for prolonged use as a near-infrared light source. Additionally, as the operating current increased from 20 mA to 250 mA, the operational temperature of the near-infrared pc-LED rose from 27.4 °C to 45.3 °C, which is caused by the accumulation of heat generated by the higher drive current. Such a slight temperature rise demonstrates its stable output in practical applications. In Fig. 7c, a photograph taken with a NIR camera utilizing the device as a light source is presented, the inset photo shows the device in operation using a near-infrared camera. Comparing this with the images captured by a visible light camera in Fig. 7d, it becomes evident that the NIR camera effectively captures damage on the banana's epidermis. This highlights the potential of leveraging the night-vision and penetration capabilities of NIR light for the non-destructive detection of fruits. In Fig. 7e, a photograph of a human hand covered with a NIR light source is displayed. The NIR camera captures the intricate distribution of blood vessels on the

human hand. Simultaneously, a comparison of the background images in Fig. 7e with Fig. 7f reveals that when the NIR pc-LED serves as the light source, the NIR camera can detect all colors of printed text, with darker fonts being particularly clear. These observations suggest that the NIR pc-LED constructed with $NaBaSc_{0.95}Si_2O_7$: $0.05Cr^{3+}$ holds great promise for applications in nondestructive testing and biomedicine.

3.4. Exploratory novel application of stable green ceramic pigment based on the $NaBaScSi_2O_7$: *x*Cr silicate

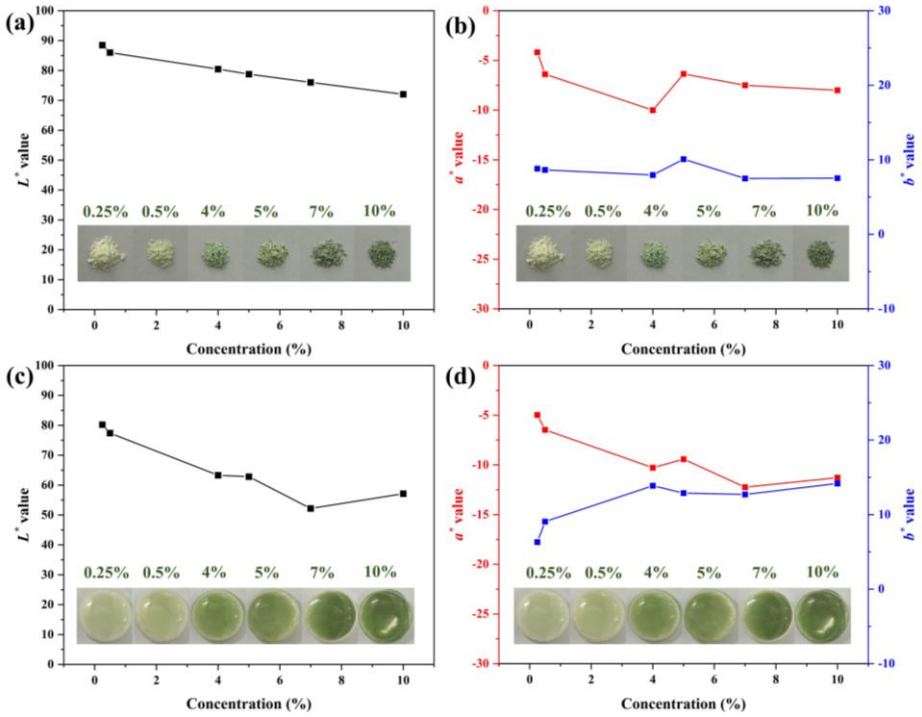

Fig. 8 (a) L^*, (b) a^*, b^* values with appearance photos of $NaBaSc_{1-x}Si_2O_7$: xCr^{3+} pigments inserted. (c) L^*, (d) a^*, b^* values with appearance photos of $NaBaSc_{1-x}Si_2O_7$: xCr^{3+} glazing samples inserted.

Fig. 8a and Fig. 8b show the values of L^*, a^* and b^* for $NaBaSc_{1-x}Si_2O_7$: xCr^{3+} samples. It can be clearly seen that with increasing Cr^{3+} doping, the L^* value of the samples gradually decreases from 88.49 to 72.03, which indicates that the brightness of the samples decreases with the increase of the Cr^{3+} content. It is known that the reflection band around 540 nm is responsible for the green color, and the intensity of the reflection band can reflect changes in the green value. As the Cr^{3+} concentration increases, the a^* value initially decreases (indicating an increase in the green value), which can be attributed to the increased reflection band intensity. However, as the concentration continues to rise to 5%, the reflection of the green region weakens, resulting in an increase in the a^* value. The value of b^*

(yellow value) shows an overall stable trend, with the increase in b^* value at the 5% concentration point likely due to the stronger absorption peak around the 360 nm region (complementary color is yellow). The trends of a^* and b^* indicate that the green value (a^*) and the yellow value (b^*) of the samples are relatively stable when the Cr^{3+} doping content changes. When the Cr^{3+} doping content is 5% (x = 0.05), the sample shows a bright light green color (L^* = 78.79, a^* = −6.36, b^* = 10.09). Fig. 8c and Fig. 8d show the values of L^*, a^* and b^* the samples glazed with $NaBaSc_{1-x}Si_2O_7$: xCr^{3+}. This step is to evaluate the color properties and the practical value as a stable green pigment. The insets are photographs of the glazing samples, the glazing surfaces exhibit a smooth and glassy surface with excellent light green hue, suggesting that the as-prepared pigments have excellent chemical and thermal stability. The overall trend of the value of L^* after firing also shows a decreasing trend when compared to the pre-firing period, and the trend of the value of a^* is similar to that of the pre-firing period, however, the b^* value shows an overall upward trend with the increase of the Cr^{3+} content. Observation of the inset shows that the prepared samples have good physicochemical and thermal stability. Additionally, the colorimetric coordination differences between the glazed samples and the powder samples are minimal, indicating that $NaBaSc_{1-x}Si_2O_7$: xCr^{3+} exhibit excellent stability as the ceramic pigments.

Conclusion

In this work, a series of $NaBaSc_{1-x}Si_2O_7$: xCr^{3+} silicates were reported, the photoluminescence and chromaticity properties were systematically investigated, and the applications in NIR pc-LED and stable green ceramic pigments were explored. The main conclusions are as follows:

(1) The phosphors show broadband NIR emission at 974 nm which is longer than most reported materials using Cr^{3+} as activator under 493 nm excitation. The underlying mechanism was attributed to the strong charge polarization caused by the intrinsic local coordination environment where Cr^{3+} are

located. The phosphors can retain 67.7% and 51.5% of room temperature intensity at 100 °C and 150 °C, respectively. NIR pc-LED device fabricated from $NaBaSc_{0.95}Si_3O_9$: $0.05Cr^{3+}$ shows promising application in night vision and non-invasive imaging.

(2) The developed $NaBaSc_{1-x}Si_2O_7$: xCr^{3+} silicate shows good color properties in the pigment powders and glazing bulk samples, which makes it a promising candidate as stable green ceramic pigment. For $NaBaSc_{1-x}Si_2O_7$: xCr^{3+} powder pigments the L^* value of gradually decreased, and the a^* and b^* values fluctuated slightly with increasing Cr^{3+}. The colorimetric coordination of the samples before and after glazing is similar, indicating that $NaBaSc_{1-x}Si_2O_7$: xCr^{3+} has excellent stability as a ceramic pigment.

Author contributions

X. J. Wang: Project administration, Writing - Original Draft and Writing - Review & Editing; S. H. Yang: Formal analysis; F. Jiang: Resources and Methodology; J. T. Wang: Investigation; C. S. Gong: Validation and Software; J.-G. Li: Conceptualization.

Conflict of Interest

The authors declare no conflict of interest.

Data Availability

All data supporting the findings of this study are available within this paper and its supplementary information.

Acknowledgements

This work is supported by the Natural Science Foundation of the Educational Department of Liaoning Province (Grant No. JYTMS20231627). Xuejiao Wang would like to thank the support from "Young Talents Project" of Jinzhou city.

References

[1] J. Zhong, C. Li, W. Zhao, S. You and J. Brgoch, *Chem. Mater.*, 2021, **34**, 337-344.

[2] M. Ferrari and V. Quaresima, *NeuroImage*, 2012, **63**, 921-935.

[3] S. Fuchi and Y. Takeda, *Phys. Status Solidi (c)*, 2011, **8**, 2653-2656.

[4] Y. Ma, X. Li, L. Wu, C. Shao, B. Zhang, T. Pang, L. Lu, H. Qiu, Y. Tian, G. Wang, Y. Hui, Q. Guo and D. Chen, *J. Adv. Ceram.*, 2024, **13**, 354-363.

[5] L. Zhang, D. Wang, Z. Hao, X. Zhang, G. Pan, H. Wu and J. Zhang, *Adv. Opt. Mater.*, 2019, **7**, 1900185.

[6] C. Lee, Z. Bao, M. Fang, T. Lesniewski, S. Mahlik, M. Grinberg, G. Leniec, S. M. Kaczmarek, M. G. Brik, Y. T. Tsai, T. L. Tsai and R. Liu, *Inorg. Chem.*, 2019, **59**, 376-385.

[7] H. Cai, S. Liu, Z. Song and Q. Liu, *J. Mater. Chem. C*, 2021, **9**, 5469-5477.

[8] J. Qi, W. Qiao and Z. Wang, *Chem. Rec.*, 2016, **16**, 1531-1548.

[9] D. Hayashi, A. M. van Dongen, J. Boerekamp, S. Spoor, G. Lucassen and J. Schleipen, *Appl. Phys. Lett.*, 2017, **110**, 233701.

[10] X. Zhou, W. Geng, J. Li, Y. Wang, J. Ding and Y. Wang, *Adv. Opt. Mater.*, 2020, **8**, 1902003.

[11] S. Wang, R. Pang, T. Tan, H. Wu, Q. Wang, C. Li, S. Zhang, T. Tan, H. You and H. Zhang, *Adv. Mater.*, 2023, **35**, 2300124.

[12] K. Oshima, K. Terasawa, S. Fuchi and Y. Takeda, *Phys. Status Solidi (c)*, 2012, **9**, 2340-2343.

[13] S. Fuchi, Y. Shimizu, K. Watanabe, H. Uemura and Y. Takeda, *Appl. Phys. Express*, 2014, **7**, 072601.

[14] A. Zabiliūtė, S. Butkutė, A. Žukauskas, P. Vitta and A. Kareiva, *Appl. Opt.*, 2014, **53**, 907-914.

[15] L. Yuan, Y. Jin, H. Wu, K. Deng, B. Qu, L. Chen, Y. Hu and R. Liu, *ACS Appl. Mater. Interfaces*, 2022, **14**, 4265-4275.

[16] E. Pan, G. Bai, L. Lei, J. Zhang and S. Xu, *J. Mater. Chem. C*, 2019, **7**, 4320-4325.

[17] Y. Wang, G. Liu and Z. Xia, *Laser Photonics Rev.*, 2024, **18**, 2300717.

[18] G. Yu, W. Wang and C. Jiang, *Ceram. Int.*, 2021, **47**, 17678-17683.

[19] Y. Jin, Z. Zhou, R. Ran, S. Tan, Y. Liu, J. Zheng, G. Xiang, L. Ma and X. Wang, *Adv. Opt. Mater.*, 2022, **10**, 2202049.

[20] X. Zou, X. Wang, H. Zhang, Y. Kang, X. Yang, X. Zhang, M. S. Molokeev and B. Lei, *Chem. Eng. J.*, 2022, **428**, 132003.

[21] T. Gao, W. Zhuang, R. Liu, Y. Liu, X. Chen and Y. Xue, *J. Alloys Compd.*, 2020, **848**, 156557.

[22] L. Pan, R. Lu, Q. Zhu, J. M. McGrath and K. Tu, *Postharvest Biol. Technol.*, 2015, **102**, 42-50.

[23] Kenry, Y. Duan and B. Liu, *Adv. Mater.*, 2018, **30**, 1802394.

[24] J. Xiang, X. Zhou, X. Zhao, Z. Wu, C. Chen, X. Zhou and C. Guo, *Laser Photonics Rev.*, 2023, **17**, 2200965.

[25] Z. Wu, J. Xiang, C. Chen, Z. Li, X. Zhou, Y. Jin and C. Guo, *Ceram. Int.*, 2024, **50**: 5242-5249.

[26] J. Wang, C. Gong, S. Yang, Q. Zhu, X. Wang and J.-G. Li, *J. Rare Earths*, 2024, **42**, 1447-1457.

[27] S. Miao, Y. Liang, Y. Zhang, D. Chen and X. Wang, *Adv. Mater. Technol.*, 2022, **7**, 2200320.

[28] P. Dang, Y. Wei, D. Liu, G. Li and J. Lin, *Adv. Opt. Mater.*, 2023, **11**, 2201739.

[29] M. Wierzbicka-Wieczorek, U. Kolitsch and E. Tillmanns, *Can. Mineral.*, 2010, **48**, 51-68.

[30] C. Liu, Z. Xia, Z. Lian, J. Zhou and Q. Yan, *J. Mater. Chem. C*, 2013, **1**, 7139-7147.

[31] G. Li, Y. Wang, W. Zeng, W. Chen, S. Han, H. Guo and Y. Li, *J. Mater. Chem. C*, 2016, **4**, 3304-3312.

[32] Z. Liu, L. Zhao, X. Yang, L. Yang, H. Zhang, W. Zeng, X. Yu, J. Qiu and X. Xu, *Chem. Eng. J.*, 2020, **401**, 126119.

[33] J. C. Rendón-Angeles, Z. Matamoros-Veloza, J. L. Rodríguez-Galicia, G. Seong, K. Yanagisawa, A. Tamayo, J. Rubio and L. A. Anaya-Chavira, *Nanomaterials*, 2021, **11**, 521.

[34] M. Ardit, G. Cruciani, F. Di Benedetto, L. Sorace and M. Dondi, *J. Eur. Ceram. Soc.*, 2018, **38**, 5234-5245.

[35] F. Jiang, J. Yu, G. Feng, J. Chen, T. Wang, X. Zhang, Q. Zhang, R. Zhang, Q. Wu, Q. Hu, Y. Yu and J. Liu, *J. Eur. Ceram. Soc.*, 2023, **43**, 4179-4188.

[36] J. Hafner. *J. Comput. Chem.*, 2008, **29**, 2044-2078.

[37] R. D. Shannon, *Acta crystallogr. A*, 1976, **32**, 751-767.

[38] Z. Luo, F. Li, Q. Zhu, X. Li, X. Sun and J. Li, *J. Mater. Res. Technol.*, 2022, **18**, 4216-4227.

[39] P. R. Jubu, F. K. Yam, V. M. Igba and K. P. Beh, *J. Solid State Chem.*, 2020, **290**, 121576.

[40] C. Wang, Y. Zhang, X. Han, D. Hu, D. He, X. Wang and H. Jiao, *J. Mater. Chem. C*, 2021, **9**, 4583.

[41] Q. Zhang, D. Liu, Z. Wang, P. Dang, H. Lian, G. Li and J. Lin, *Adv. Opt. Mater.*, 2023, **11**, 2202478.

[42] Q. Pang, Y. Wang, L. Yan, G. Zhu, S. Xu, J. Zhang, X. Zhang, Y. Cao and B. Chen, *Laser Photonics Rev.*, 2024, **18**, 2301039.

[43] S. Miao, Y. Liang, Y. Zhang, D. Chen and X. Wang, *ACS Appl. Mater. Interfaces* 2021, **13**, 36011-36019.

[44] J. Zhang, X. Li and G. Chen, *Mater. Chem. Phys.* 2018, **206**, 40-47.

[45] K. Li and D. Xue, *J. Phys. Chem.*, 2006, **110**, 11332-11337.

[46] Z. Yang, Y. Zhao, Y. Zhou, J. Qiao, Y. Chuang, M. S. Molokeev and Z. Xia, *Adv. Funct. Mater.*, 2022, **32**, 2103927.

[47] Y. Li, S. Fang, Q. Zhu, S. Li, B. Liu, F. Feng, R. Xie and L. Wang, *Laser Photonics Rev.* **2024**, *18* (5), 2300915.

[48] Y. Liu, F. Di Stasio, C. Bi, J. Zhang, Z. Xia, Z. Shi and L. Manna, *Adv. Mater.*, 2024, 36, 2312482.

[49] F. Zhu, Y. Gao, B. Zhu, L. Huang and J. Qiu, *Chem. Eng. J.*, 2024, **479**, 147568.

[50] J. Wang, L. Jiang, R. Pang, S. Zhang, D. Li, K. Li, C. Li and H. Zhang, *Inorg. Chem. Front.*, 2022, **9**, 2240-2251.

[51] X. Ding, Q. Zhang, Z. Li and Y. Min, *J. Mater. Chem. C*, 2021, **9**, 16022-16032.

[52] D. Liu, G. Li, P. Dang, Q. Zhang, Y. Wei, H. Lian, M. Shang, C.-C. Lin and J. Lin, *Angew. Chem. Int. Edit.* 2021, **60**, 14644-14649.

[53] Q. Zhang, D. Liu, P. Dang, H. Lian, G. Li and J. Lin, *Laser Photonics Rev.* 2022, **16**, 2100459.

[54] S. Miao, Y. Liang, Y. Zhang, D. Chen, X. Wang, *Adv. Mater. Technol.* 2022, **7**, 2200320.